

## CALL FOR PAPERS | *Neurophysiology of Tactile Perception: A Tribute to Steven Hsiao*

### Tactile signals transmitted by the vibrissa during active whisking behavior

Lucie A. Huet,<sup>1</sup> Christopher L. Schroeder,<sup>2</sup> and Mitra J. Z. Hartmann<sup>1,2</sup>

<sup>1</sup>Department of Mechanical Engineering, Northwestern University, Evanston, Illinois; and <sup>2</sup>Department of Biomedical Engineering, Northwestern University, Evanston, Illinois

Submitted 7 January 2015; accepted in final form 30 March 2015

**Huet LA, Schroeder CL, Hartmann MJ.** Tactile signals transmitted by the vibrissa during active whisking behavior. *J Neurophysiol* 113: 3511–3518, 2015. First published April 1, 2015; doi:10.1152/jn.00011.2015.—The rodent vibrissal-trigeminal system is one of the most widely used models for the study of somatosensation and tactile perception, but to date the field has been unable to quantify the complete set of mechanical input signals generated during natural whisking behavior. In this report we show that during whisking behavior of awake rats (*Rattus norvegicus*), the whisker will often bend out of its plane of rotation, generating sizeable mechanical (tactile) signals out of the plane. We then develop a model of whisker bending that allows us to compute the three-dimensional tactile signals at the vibrissal base during active whisking behavior. Considerable information can be lost if whisking motions are considered only in two dimensions, and we offer some suggestions for experimentalists concerned with monitoring the direction of bending. These data represent the first quantification of the physical signals transmitted to the mechanoreceptors in the follicle during active whisking behavior.

active sensing; biomechanics; somatosensation; trigeminal; whisker

RODENT WHISKING BEHAVIOR is often used as a model to study somatosensation, but we do not yet fully understand the sensory input parameters generated when a whisker touches an object. Currently, the standard way to characterize active whisking touch is through the horizontal angle and radial distance of contact (Mehta et al. 2007; O'Connor et al. 2010; Szwed et al. 2003). However, this approach does not capture the contribution of the complex three-dimensional (3D) shape and mechanics of the whisker as it transmits information from the point of contact to the follicle. Global curvature (Bagdasarian et al. 2013) begins to approximate whisker bending but cannot uniquely represent whisker shape.

The most complete measure of input to the vibrissal-trigeminal system is the 3D set of forces and moments at the whisker base. The deflection of a whisker as it contacts an object produces these forces and moments, which cause deformations of the mechanoreceptors in the vibrissa follicle (Ebara et al. 2002). However, it is not possible to measure these forces and moments experimentally; they must be computed with mechanical models.

Previous studies have developed two-dimensional (2D) mechanical models of whiskers (Bagdasarian et al. 2013; Hires et al. 2013; Kaneko et al. 1998; Pammer et al. 2013; Solomon and Hartmann 2006, 2010, 2011). It is well established, however, that neurons of the trigeminal system are exquisitely sensitive to 3D deflection (Furuta et al. 2006; Jones et al. 2004; Lichtenstein et al. 1990; Simons 1978, 1985). Thus, if whisking behavior involves substantial deflection out of the plane of motion, 2D models will fail to capture significant information transmitted to the nervous system.

In this article we show that the whisker will, in fact, often bend out of its plane of rotation, and we then develop a 3D model of whisker bending to compute the full set of tactile signals at the vibrissal base. We then assess how much the 3D tactile signals during active whisking differ from those obtained in a 2D analysis. The results are the first complete quantification of the physical signals transmitted to the follicle during whisking behavior of awake animals.

#### MATERIALS AND METHODS

**Three-dimensional bending model.** A numerical model of 3D whisker bending was developed based on principles from previous studies (Kaneko et al. 1998; Quist and Hartmann 2012; Solomon and Hartmann 2006). The whisker is represented as a series of rigid links connected by nodes that allow rotation in all three dimensions, and the motion of each node is constrained by (rotational) springs. The system is quasistatic and frictionless, so there are no inertial effects and the applied force always remains normal to the whisker.

The model operates in vibrissa-centered coordinates. The origin is at the vibrissa base, and the  $x$ -axis is defined to be coincident with the vibrissa as it emerges from the mystacial pad. To account for the vibrissa's intrinsic curvature, the  $y$ -axis is defined so that the planar region of the vibrissa, i.e., the proximal ~60–70% (Knutson et al. 2008), lies in the  $x$ - $y$  plane and the vibrissal tip points in the positive  $y$ -direction.

As shown in Fig. 1A, when a rat whisks against a peg, the vibrissa will contact the peg at a single point ( $r_{cp}$ ,  $\theta_{cp}$ ,  $\varphi_{cp}$ ). The peg exerts a force on the whisker at the contact point, and this force is balanced by equivalent vectors ( $\mathbf{F}$ ) and moment ( $\mathbf{M}$ ) at the whisker base.  $\mathbf{F}$  and  $\mathbf{M}$  each have three components:  $F_x$ ,  $F_y$ ,  $F_z$ , and  $M_x$ ,  $M_y$ ,  $M_z$ . The component  $F_x$  acts along the axis of the vibrissa at the base, and the components  $F_y$  and  $F_z$  comprise the transverse force. The components  $M_y$  and  $M_z$  are bending moments, whereas the third moment,  $M_x$ , twists the vibrissa about its own axis. These six signals represent all mechanical information transmitted by the whisker to the neurons of the trigeminal ganglion (Jones et al. 2004; Leiser and Moxon 2007; Lichtenstein et al. 1990).

Address for reprint requests and other correspondence: M.J.Z. Hartmann, Mechanical Engineering Dept., Northwestern Univ., 2145 Sheridan Rd., Evanston, IL 60208 (e-mail: hartmann@northwestern.edu).

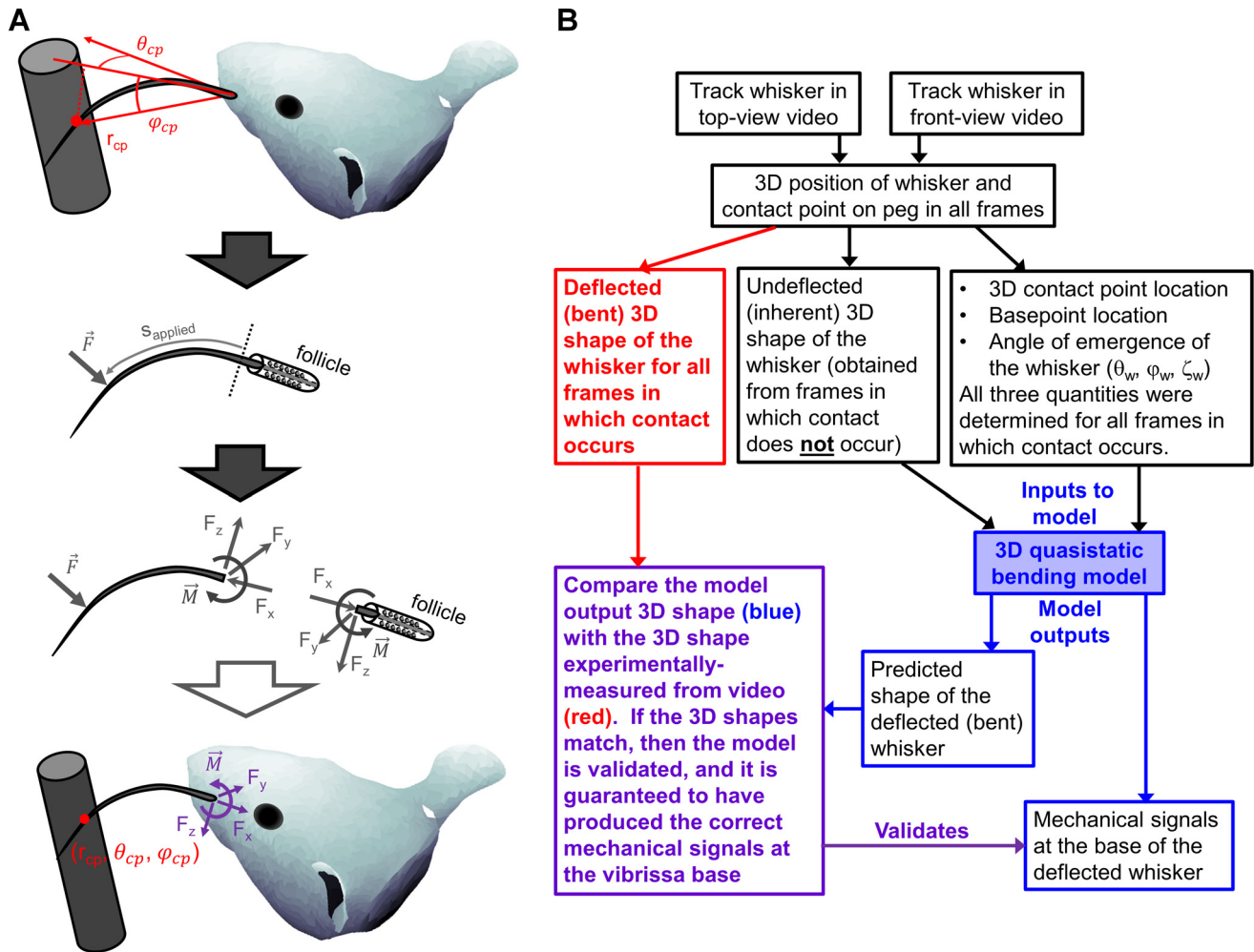


Fig. 1. Methods for computing mechanical signals at the vibrissal base. **A**: contact between a peg and a whisker at location  $(r_{cp}, \theta_{cp}, \varphi_{cp})$  creates a point force ( $\vec{F}$ ) on the whisker that causes the whisker to bend. The location of the contact point (subscript “cp”) is defined relative to the vibrissa base such that  $r_{cp}$  is the Euclidean distance from the whisker base to the contact point,  $\theta_{cp}$  is the azimuthal angle to the contact point, and  $\varphi_{cp}$  is the elevation angle to the contact point. Note that  $r_{cp}$  is not the arc length at which the whisker makes contact with the peg, which is shown as  $s_{applied}$ . The applied force  $\vec{F}$  generates a force vector and a moment vector at the whisker base. Both of these vectors have 3 components; the 3 components of the force ( $F_x, F_y, F_z$ ) are shown. As conceptually summarized at *bottom*, whisker deflection to a contact point location  $(r_{cp}, \theta_{cp}, \varphi_{cp})$  results in 3-dimensional (3D) reaction force and moments at the base. **B**: flowchart depicting the calculation and validation of  $[\mathbf{F}, \mathbf{M}]$  at the vibrissal base as an awake rat whiskered against a peg. *Step 1* (top 2 rows of boxes): the vibrissa and contact point were tracked in the 2 orthogonal camera views and then merged to obtain a full 3D reconstruction of vibrissal shape, position, and orientation as well as contact point location. *Step 2* (third row, black boxes): *left* black box shows that for each whisk against the peg, the 3D undeflected, intrinsic whisker shape was defined by the frame in which the whisker initially made or broke contact; *right* black box shows that for each frame in which contact occurred, we measured the 3D contact point location  $(r_{cp}, \theta_{cp}, \varphi_{cp})$  of the whisker on the peg, as well as the whisker base point location and the whisker angle of emergence  $(\theta_w, \varphi_w, \zeta_w)$ . Note that none of these measured quantities provide any information about the deflected shape of the whisker. *Step 3a* (red box): the 3D deflected shape of the whisker was measured experimentally. *Step 3b* (shaded blue box and its outputs): the model predicted the 3D deflected shape of the whisker as well as  $[\mathbf{F}, \mathbf{M}]$  at the vibrissal base. *Step 4* (purple box): comparing the 3D shape of the whisker predicted by the model with the 3D shape measured experimentally validated (purple arrow) the calculation of  $[\mathbf{F}, \mathbf{M}]$ .

The model uses the force exerted on the whisker to calculate a moment vector at each of the nodes between the links. The component  $M_x$  for each link points directly along the axis of that link, and  $M_b = \sqrt{M_y^2 + M_z^2}$  represents the total bending moment. At each node, the spring deflects both in response to the bending moment and in response to the applied torque according to the following equations:

For bending moment,

$$dk = \frac{M_b}{EI} \tag{1}$$

$$d\theta = (dk)(ds), \tag{2}$$

where  $dk$  is the change in curvature,  $M_b$  is the applied bending moment,  $E$  is Young’s modulus, and  $I$  is the area moment of inertia determined by

the whisker’s radius at that node ( $I = \pi r^4/4$ ). Because all link lengths are equal, we can apply Eq. 2 so that  $d\theta$  (the change in angle at each node in the plane of the bending moment) is equal to the product of  $ds$  (the link length) and  $dk$  (the change in curvature at that node).

For torque,

$$d\varphi = \frac{\tau ds}{GJ}, \tag{3}$$

where  $d\varphi$  is the change in angle about the link’s own axis,  $\tau$  is the applied torque,  $ds$  is the link length,  $G$  is the shear modulus, and  $J$  is the polar area moment of inertia.

The deflections of Eqs. 1–3 are applied at every node, and the force and moment vectors that result at the node at the base are denoted as  $[\mathbf{F}, \mathbf{M}]$ .

As a rat whisks against a peg, the force exerted on the whisker is unknown. Thus in the present work the model used the MATLAB function `fminsearch` (Nelder-Mead algorithm) to optimize over three parameters: 1) the magnitude of the applied force ( $F_{\text{applied}} = \|\mathbf{F}\|$ ), 2) the orientation about the whisker at which the force is applied, and 3) the arc length along the whisker at which the force is applied ( $s_{\text{applied}}$ ). For each guess of these three parameters, the model solved for the whisker's deflected shape, including the location of the contact point on the whisker. The optimization minimizes the Euclidean distance between this point and the user-specified vibrissa-object contact point ( $r_{\text{cp}}$ ,  $\theta_{\text{cp}}$ ,  $\varphi_{\text{cp}}$ ). A solution is found when this distance reaches zero, and the model then solves for  $[\mathbf{F}, \mathbf{M}]$  at the base node. Note that  $s_{\text{applied}}$  is not the same as  $r_{\text{cp}}$  because  $s_{\text{applied}}$  is the arc length from whisker base to contact point, whereas  $r_{\text{cp}}$  is the straight line distance from whisker base to contact point.

**Quantifying whisking behavior.** All procedures were approved by Northwestern's Animal Care and Use Committee. Behavioral data were obtained during 15 bouts of whisking (60.17 s total) from 7 female Long-Evans rats ages 3–6 mo. Only one whisker on one side of the face was monitored in 3D; all other whiskers on that side were trimmed to the level of the fur. The monitored whiskers were gamma, C1, E1, B2, C2, E2, and B3. Rats were not head-restrained but were body-restrained so that whiskers remained in the field of view. Two Photron 1024PCI monochrome cameras (1,000 fps, shutter speed 1/3000 s, lenses Nikon AF Micro-Nikkor 60 mm) were mounted orthogonally an equal distance ( $\sim 60$  cm) from the rat. Pixel length (58  $\mu\text{m}$ ) was matched between the cameras using a  $2 \times 2\text{-mm}^2$  checkerboard grid. The top-down view of the whisker was tracked using the open-source software Whisk (Clack et al. 2012), whereas the front-on view and the contact point were tracked manually. To perform 3D merging the nodes of the 2D tracked whiskers were splined and interpolated such that one node appeared per  $x$ -pixel. Because the pixels matched between cameras, the two tracked whiskers ( $x$ - $y$  nodes in top view,  $x$ - $z$  nodes in front view) could be combined into a single 3D whisker (Hartley and Zisserman 2003).

**Using the model to compute  $[\mathbf{F}, \mathbf{M}]$  based on behavioral data.** Parameters for the whisker in the model were based on typical values: a base diameter of 100  $\mu\text{m}$  and taper (base radius/tip radius) of 15 (Hires et al. 2013; Williams and Kramer 2010) yields a tip diameter of 6.67  $\mu\text{m}$ . Young's modulus was 3.3 GPa (Quist et al. 2011), and the shear modulus  $G$  was obtained by inserting Poisson's ratio for keratin,  $\nu = 0.38$  (Etnier 2003), into the following equation:

$$G = \frac{E}{2(1 + \nu)}, \quad (4)$$

Figure 1B outlines the steps used to compute  $\mathbf{F}$  and  $\mathbf{M}$  during active whisking behavior and to validate the model. The output of the model (shaded blue box in Fig. 1B) predicted the 3D shape of the deflected whisker as well as  $[\mathbf{F}, \mathbf{M}]$  at the whisker base. The predicted 3D whisker shape was compared with the experimentally measured 3D whisker shape (red box in Fig. 1B). The theory of elasticity guarantees that if the two 3D shapes match, the model has produced the correct mechanical signals at the vibrissal base, and the model is validated (Hartog 1987).

One subtlety requires mention. During contact, the roll of the whisker ( $\zeta_w$ ) is dramatically distorted from the whisker's free-air path (Knutsen et al. 2008). Thus the undeflected value of  $\zeta_w$  that would have occurred cannot be measured directly during frames of contact. We therefore exploited the tightly linear relationship between  $\zeta_w$  and protraction angle  $\theta_w$  (Knutsen et al. 2008). In each trial we used the  $\zeta_w$  angles tracked during noncontact frames and computed the linear relationship between  $\zeta_w$  and protraction angle; for example,  $\Delta\zeta_w = -0.636(\Delta\theta)$ .

The model was validated against previously published 2D models (Quist et al. 2014; Solomon and Hartmann 2006) to within numerical error. Error between experiment and simulation was quantified as the

absolute value of the Euclidean distance between the tracked whisker and model output. Error was averaged over every node on the whisker between the base point and the contact point.

## RESULTS

We tracked 3D whisker motion as awake, body-restrained rats whisked against a peg. The magnitude of vertical motion of the whisker on the peg varied considerably from whisk to whisk. Figure 2A illustrates the largest range of vertical motion during a single whisk observed during a 3.3-s whisking bout. Vertical motion during each whisk ranged from 400  $\mu\text{m}$  to 6.8 mm, and the total range of motion (across all 26 whisks in the bout) was 12 mm. These vertical motions were nearly invisible in the top-down camera view.

These effects are generalized over all 7 rats, for all 15 whisking bouts, in Table 1 and in the histogram shown in Fig. 2B. Overall, 57.8% (174/301) of whisks exhibited vertical slip less than 1 mm, whereas 17.9% (54/301) exhibited vertical slip 2 mm or greater and  $\sim 7.0\%$  (21/301) exhibited vertical slip 4 mm or greater. The histogram in Fig. 2B also reveals that all seven rats exhibited whisks with vertical slip greater than 1 mm, although only three of the seven rats exhibited whisks with slip greater than 4 mm.

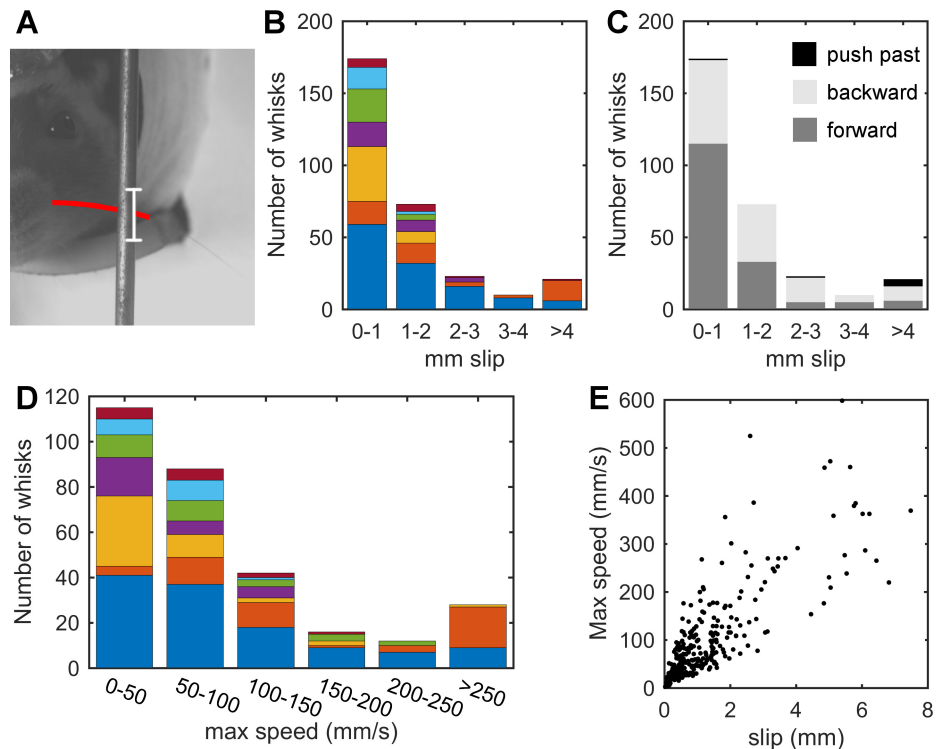
During experiments, the rat could either whisk forward against the peg, as happened during 164/301 (54.4%) whisks, or backward against the peg (130/301 whisks; 43.2%), or the rat could push its whisker past the peg (7/301 whisks; 2.3%). Vertical slips of all magnitudes occurred when the rat was whisking in either direction against the peg (Fig. 2C). Additionally, as might be expected, vertical slip tended to be particularly large when the whisker pushed past the peg. Notably, however, one push past the peg occurred with vertical slip less than 1 mm, so the "pushing-past" motion is not invariably associated with large vertical slip.

Given that whisker velocity is a key parameter that underlies neural responses at all levels of the trigeminal system, the vertical slip velocity was quantified as the first derivative of the  $z$ -slip position. Maximum slip speeds (maximum of the absolute value of the velocity) are tabulated in Table 1, and a histogram of these speeds is shown in Fig. 2D. Maximum slip speeds generally ranged between 2.9 and 600 mm/s with a median of 67.6 mm/s (2 outlier points had speeds  $> 600$  mm/s). The speed of the vertical slip was found to correlate approximately linearly with slip magnitude ( $r^2 = 0.62$ ), as shown in Fig. 2E. Thus the amount of slip in the  $z$ -direction is also indicative of the speed of the slip in this direction.

The changes in deflection direction associated with 1-mm slip and the typical maximum speeds associated with the slip on each whisk (median 67.6 mm/s) are well above threshold to generate and modulate responses in neurons all along the trigeminal pathway, including S1 (Jones et al. 2004; Lichtenstein et al. 1990; Simons 1978, 1985). The results shown in Fig. 2 thus all point to the necessity of studying vibrissal motion and bending in 3D.

We therefore developed a 3D model of whisker bending (see MATERIALS AND METHODS) to compute the complete set of tactile signals during whisking behavior against the peg. Following the flowchart of Fig. 1B, we provided the model with the undeflected shape of the vibrissa and the contact point in each video frame. The model outputs were  $[\mathbf{F}, \mathbf{M}]$  at the whisker base and the deflected shape of the vibrissa after it had bent

Fig. 2. Magnitude of the whisker's vertical motion along the peg is characterized by large whisk-to-whisk variability. **A**: single frame from the front camera view of a rat whisking against a peg. The whisker is outlined in red for visual clarity. Over the course of the 3.3-s whisking bout, the smallest vertical slip distance along the peg was 400  $\mu\text{m}$ , comparable to the width of the red whisker outline. The largest vertical slip distance was 6.8 mm, illustrated as the white bar. Both small and large vertical motions were effectively unobservable in the top-down camera view. **B**: histogram of the magnitude of the vertical slip across all 7 rats (each coded a different color), 15 bouts of whisking, and 301 whisks. Data corresponding to this histogram are given in Table 1. **C**: whisker slip occurred regardless of whether the rat whisked forward or backward against the peg. Whisks in which the whisker pushed past the peg were disproportionately represented in whisks with slip  $>4$  mm (5/21 whisks; 23.8%). **D**: histogram of the maximum slip speed for each of the 301 whisks. Data from each rat are color coded as in **B**. Data corresponding to this histogram are also provided in Table 1. **E**: as expected, maximum slip speed is positively correlated with slip magnitude, so whisks that exhibit large vertical slip will generally experience large speeds in this direction, as well. Two outlier data points (speeds  $>600$  mm/s) have been omitted from this graph.



against the peg. All six mechanical signals over the 3.3-s whisking bout are shown in Fig. 3A and Supplemental Video 1 (supplemental data for this article is available online at the Journal of Neurophysiology website).

In each frame, model results were confirmed by comparing the 3D vibrissal shape as measured experimentally with the 3D vibrissal shape predicted by the model. As described in Fig. 1B, if the 3D shape of the whisker matches between the model and experiment, then  $[F, M]$  at the base are guaranteed to have been determined correctly (Hartog 1987). The overall excellent match between model and experiment is shown in the *bottom* trace of Fig. 3A. For this trial, the average distance between experimentally measured and simulated vibrissal shape was 58  $\mu\text{m}$ . When averaged across all contact frames, the maximum error across all nodes of the whisker was 117  $\mu\text{m}$ . These averages do not include frames in which the whisker did not

contact the peg, for which the error is zero by definition. The model was tested on three whisking bouts from two of the seven rats. Together, the three bouts lasted 8,431 ms and included 2,760 ms of whisker-peg contact. Across all contact frames, the average error over whisker arc length was 93.7  $\mu\text{m}$ , and the average maximum error was 180  $\mu\text{m}$ . These errors are on the order of the diameter of the whisker near its base, meaning the errors are very small.

Two specific examples of the quality of fit are shown in Fig. 3B, which illustrates the two orthogonal views of the whisking rat as well as the 3D merged whisker and the corresponding output of the model. The *top* row of Fig. 3B depicts a frame of the undeflected whisker shape ( $t = 775$  ms). The next two rows show frames in which deflection occurred, one in which the rat whisked forward against the peg ( $t = 1,280$  ms) and one in which the rat whisked backward against the peg ( $t = 2,943$  ms). For these two frames, the mean errors between experiment and model were 71 and 47  $\mu\text{m}$ , and maximum errors were 119 and 88  $\mu\text{m}$ , respectively. The 3D merged whisker shown in the *right* column of Fig. 3B provides intuition for these error magnitudes: the simulation results (cyan) overlay the experimental data (red) nearly exactly.

Finally, Fig. 4 assesses how much the 3D tactile signals of Fig. 3 differ from those that would have been obtained from a 2D analysis. The most obvious difference, shown in Fig. 4A, is that the 3D analysis has three more traces than the 2D analysis. The 3D case contains both  $F_{y3D}$  and  $F_{z3D}$ , as well as  $M_{y3D}$  and  $M_{z3D}$ , whereas in 2D these coalesce into a single transverse force ( $F_{T2D}$ ) and a single bending moment ( $M_{B2D}$ ). The 3D analysis also includes the “twisting” moment,  $M_x$ , which is missing in the 2D analysis.

Turning now to similarities between the 3D and 2D analyses, the trace that is most similar between the 3D and 2D conditions is the axial force,  $F_x$ . We also see that, at least for

Table 1. Slip magnitudes and speeds per whisk

	No. of whisks (%)
<b>z-Slip magnitudes</b>	
Slip $\leq 0.5$ mm	96 (31.9%)
Slip $\leq 1.0$ mm	174 (57.8%)
$1.0 < \text{Slip} \leq 2.0$ mm	73 (24.3%)
$2.0 < \text{Slip} \leq 3.0$ mm	23 (7.64%)
$3.0 < \text{Slip} \leq 4.0$ mm	10 (3.32%)
Slip $> 4.0$ mm	21 (6.98%)
<b>Maximum z-slip speeds</b>	
Slip speed $\leq 50$ mm/s	115 (38.2%)
$50 < \text{Slip speed} \leq 100$ mm/s	88 (29.2%)
$100 < \text{Slip speed} \leq 150$ mm/s	42 (14.0%)
$150 < \text{Slip speed} \leq 200$ mm/s	16 (5.32%)
$200 < \text{Slip speed} \leq 250$ mm/s	12 (3.99%)
Slip speed $> 250$ mm/s	28 (9.30%)

Magnitudes and maximum speeds of the vertical slip (z-slip) are indicated by number (percentage in parentheses) for all 301 whisks.

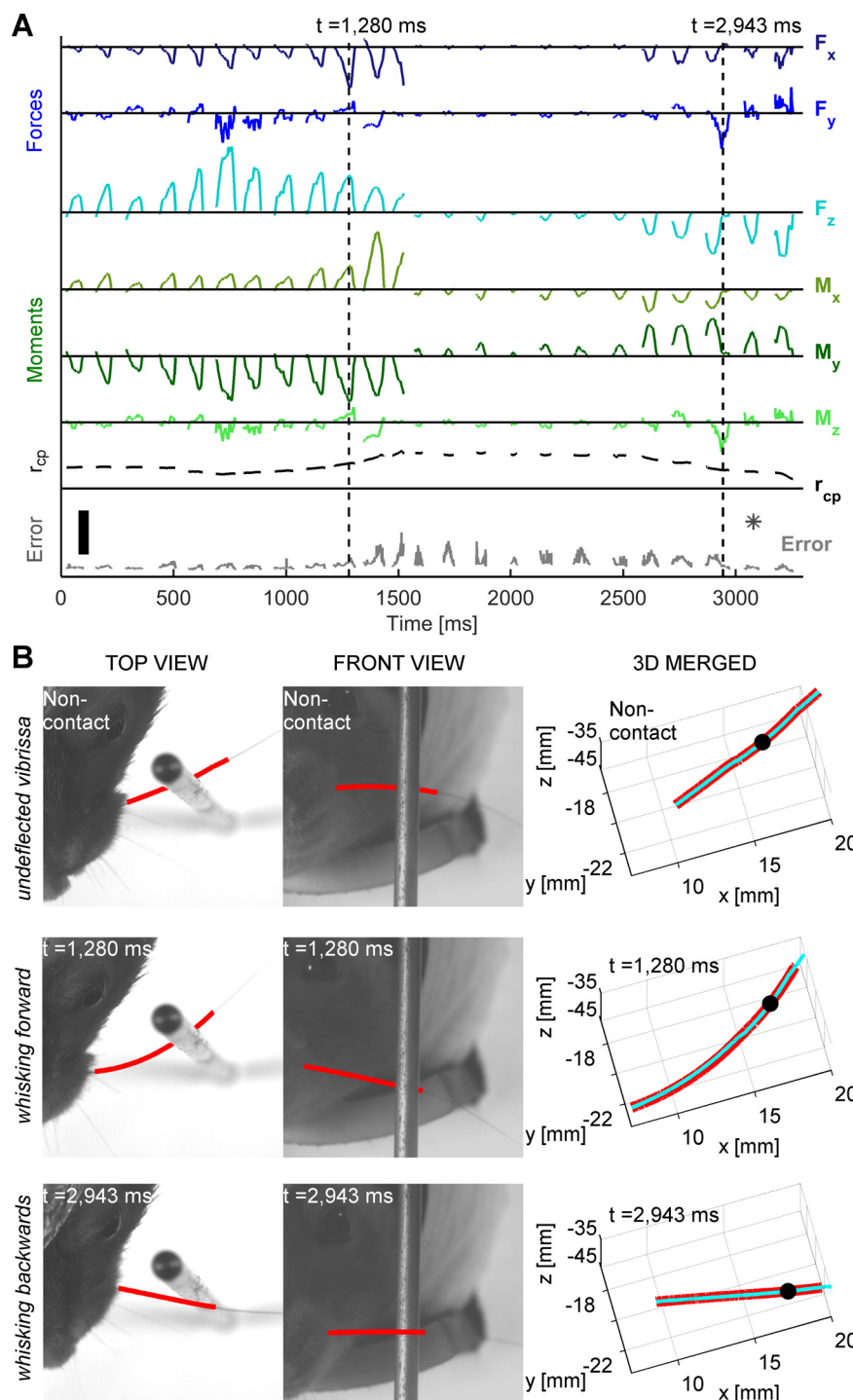


Fig. 3. All 6 mechanotactile signals available to the rat during active whisking behavior. **A**: all components of force and moment generated at the whisker base as well as  $r_{cp}$  and error for 3,300 ms of whisking, including 1,661 ms of vibrissal-peg contact. All mechanical signals have been filtered at 85 Hz. From *top to bottom*, the traces represent  $F_x$ , the axial force;  $F_y$  and  $F_z$ , the 2 components of transverse force;  $M_x$ , the “twisting” moment about the vibrissa’s axis;  $M_y$  and  $M_z$ , the 2 components of bending moment;  $r_{cp}$  (“radial distance”), the distance from the whisker base to the contact point of the whisker on the peg; and mean error. Mean error has not been filtered and was quantified as the mean of the Euclidean distance between experimentally measured and simulated vibrissal shape across the whisker arc length from the base point to the contact point. The largest errors, on the order of 200  $\mu\text{m}$ , occur between frames 1,300 and 2,000, which are times when the whisker slips past the peg and experiences large inertial forces. Dynamic models are needed to capture these inertial effects. The asterisk in the error signal at 3,078 ms represents a single outlier point with an error of 358  $\mu\text{m}$ . Scale bar: 1.0 mN for  $F_y$  and  $F_z$ , 0.5 mN for  $F_x$ , 10  $\mu\text{N}\cdot\text{m}$  for  $M_y$  and  $M_z$ , 2.0  $\mu\text{N}\cdot\text{m}$  for  $M_x$ , 20 mm for  $r_{cp}$ , and 200  $\mu\text{m}$  for mean error. The labeled vertical dashed lines indicate times of the frames shown in **B**. **B**: examples of the quality of the experiment-simulation match. *Left* and *center* columns show the front and top camera views with the whisker tracked in red; *right* column shows the 3D tracked vibrissa in red with the 3D model output overlaid in cyan, and the black dots are the 3D locations of the contact point. The 3 rows illustrate whisker shapes at 3 different times during the trial shown in **A**. The undeflected whisker shape is shown in the *top* row. The shape of the whisker as it deflects forward ( $t = 1,280$  ms) and backward ( $t = 2,943$  ms) against the peg is shown in the *middle* and *bottom* rows. The 3D shape of the deflected whisker as predicted from simulation (blue) is a good match to the shape of the experimentally tracked whisker (red).

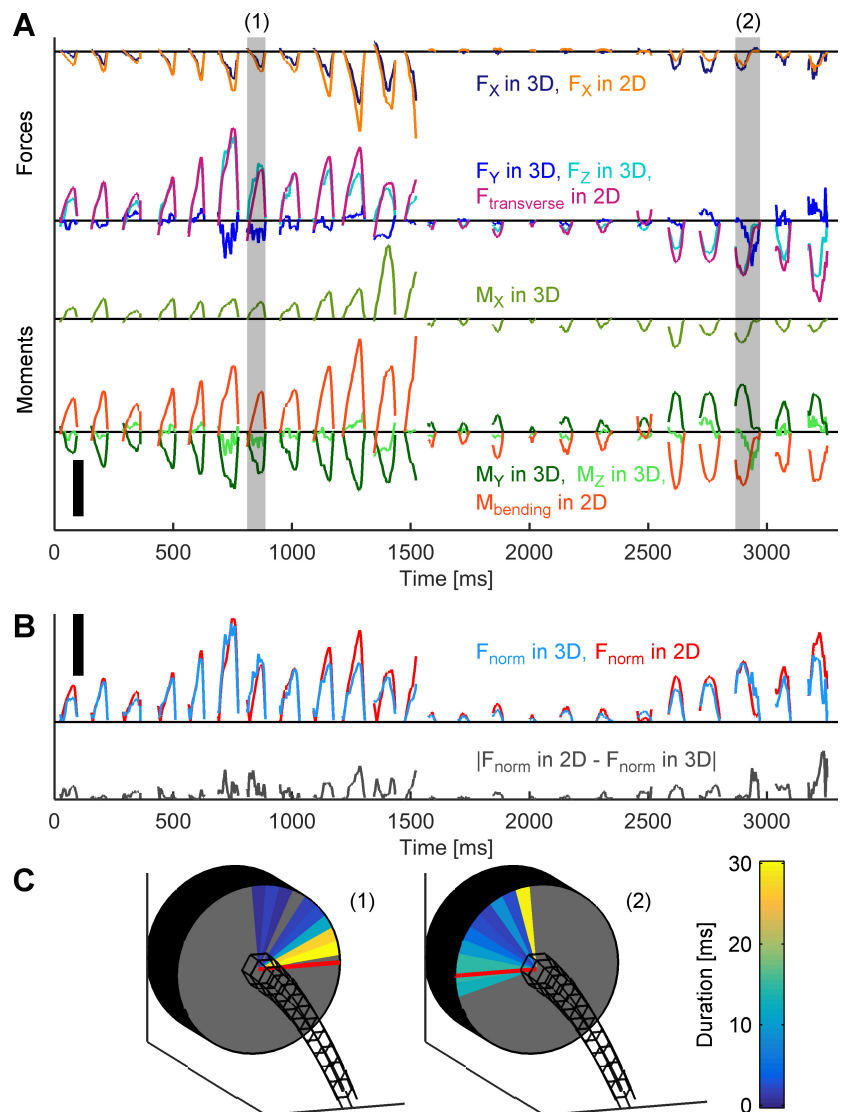
the particular example shown,  $F_{z3D}$  matches fairly closely with the 2D transverse force,  $F_{T2D}$ , and the magnitude of  $M_{y3D}$  matches fairly closely with the magnitude of the 2D bending moment,  $M_{B2D}$ .

Further similarities between 2D and 3D analysis are observed by comparing the norms of the 2D and 3D signals: Fig. 4B shows that these traces are remarkably similar. Interestingly, the 2D signal magnitude is actually larger than the 3D signal magnitude. This may seem unintuitive, but the insight is that the whisker is twisting about its own axis in 3D. In 2D conditions this torque is not possible, so a larger force is

needed to bend the whisker into the same top-down shape as was generated by the 3D torque. Overall, however, it is clear that the magnitude of the 3D deflection is sometimes well approximated by the magnitude of the 2D deflection. The exact conditions under which this approximation holds require further study. The key point, however, is that even in cases when 2D magnitude is a good approximation for 3D magnitude, the 2D analysis omits three components:  $F_{y3D}$ ,  $M_{z3D}$ , and  $M_{x3D}$ .

One of the largest effects of this omission is that the deflection direction will be misrepresented in 2D. To illus-

Fig. 4. Significant information is lost in a 2D, compared with a 3D, analysis. **A**: analysis of the 3D whisker trajectory yields 3 more dimensions than the 2D analysis. The 3D force and moment traces, shown in shades of green and blue, are identical to those shown in Fig. 3. The corresponding 2D force and moment traces are shown in shades of red and orange. Although 2D and 3D analyses provide relatively similar results for axial force ( $F_x$ ), all other traces are very different.  $M_x$  does not even exist in the 2D case. Scale bar: 1.0 mN for  $F_y$ ,  $F_z$ , and  $F_{\text{transverse}}$ ; 0.5 mN for  $F_x$ ;  $10 \mu\text{N}\cdot\text{m}$  for  $M_y$ ,  $M_z$ , and bending moment ( $M_{\text{bending}}$ ); and  $2.0 \mu\text{N}\cdot\text{m}$  for  $M_x$ . The shaded areas labeled “(1)” and “(2)” indicate the deflections analyzed in **C**. **B**, *top*: comparison between the norm of the 2D force ( $F_{\text{norm}2\text{D}} = \sqrt{F_{x2\text{D}}^2 + F_{y2\text{D}}^2}$ ; red) and the norm of the 3D force ( $F_{\text{norm}3\text{D}} = \sqrt{F_{x3\text{D}}^2 + F_{y3\text{D}}^2 + F_{z3\text{D}}^2}$ ; blue). The 2 forces are similar in magnitude, although notably the 2D force is often larger. Scale bar: 1.0 mN. **B**, *bottom*: the error between the 2D and 3D force norms, as defined by the absolute value of the difference. Median percent error with respect to the norm of the 3D force is 32.2%. The mean error would be much larger due to division by small numbers. **C**: with a 3D analysis, it is possible to visualize the direction in which the whisker deflects during contact whisking. Two examples are shown for the contact periods shaded in **A**. In both examples a circular cross section of the follicle is depicted, with the whisker drawn as a mesh grid. The color of each angular “pie slice” indicates the duration (in ms) the whisker was deflected toward that angle, as calculated by  $\text{atan}(F_{z3\text{D}}/F_{y3\text{D}})$ . The red horizontal lines indicate the rostral-caudal direction deflection inherently assumed by the 2D analysis. Both plots are shown in whisker-centered coordinates.



trate this effect, we choose two example contact periods, indicated by the gray shaded regions in Fig. 4A. The directions in which the whisker is deflected in these two examples are shown in Fig. 4C. “Deflection direction” means the direction of the force at the whisker base. As illustrated in Fig. 4C, we imagine a circular cross section of the follicle with the whisker depicted as a wire mesh. The  $10^\circ$  “pie slices” shown in color in the follicle cross section indicate how often the whisker was deflected in that direction in the 3D analysis. In the corresponding 2D analysis, the deflection direction can only be directly rostral-caudal, depicted as red horizontal lines in Fig. 4C.

In Fig. 4, the contact period marked “(1)” illustrates a typical contact period. The general direction of the deflection is rostral-caudal, although significant deflection happens up to  $20^\circ$  (orange pie slice). The contact period marked “(2)” shows an instance in which a significant portion of the deflection happens near  $90^\circ$ , far from the rostral-caudal direction assumed by the 2D analysis. The 2D analysis thus clearly omits important information about the directionality of deflection, which will affect neural responses (Jones et al. 2004; Lichtenstein et al. 1990; Simons 1978, 1985).

## DISCUSSION

**Advantages and limitations of the 3D quasistatic model.** The present study provides the first description of the 3D tactile input signals obtained during active whisking behavior. Previous descriptions of vibrissal mechanics and geometry have been limited to two dimensions (Bagdasarian et al. 2013; Hires et al. 2013; Kaneko et al. 1998; Pammer et al. 2013; Quist and Hartmann 2012; Solomon and Hartmann 2006, 2011). Quasistatic models are simpler than dynamic models because, by definition, they do not incorporate any effects that depend on the whisker’s mass. This means that quasistatic models cannot capture the vibrations that follow a collision or signals associated with texture exploration; these require dynamic models (Boubenec et al. 2012; Quist et al. 2014; Yan et al. 2013). These studies have suggested, however, that a large component of touch-based whisking can be explained with quasistatics alone. In the present study, the small error shown in Fig. 3 indicates that a quasistatic solution simulates the whisker’s mechanics well for the behavioral conditions studied.

**Frictional effects.** Although outside the scope of the current work, informal evaluation of the present data set provided the

intuition that large 3D slip is likely to be associated with frictional effects (Boubenec et al. 2012; Pammer et al. 2013; Solomon and Hartmann 2008), including stick-slip of the vibrissa on the peg (Ritt et al. 2008; Wolfe et al. 2008).

Friction plays a large role in whisker mechanics but is challenging to study. The present model accounts for friction as the whisker slips up and down on the peg but does not account for friction along the whisker's length. To explain this asymmetric treatment, we consider what the term "frictionless" means with respect to the peg and the whisker independently. First, consider friction as the whisker slips up and down the peg. In the frictionless case, the force vector is constrained to lie in the horizontal plane, perpendicular to the peg. In the experiments of Fig. 3, however, the contact point along the height of the peg is known. Thus the force vector is no longer constrained to lie in the horizontal plane; forces can act nonnormal to the peg. These nonnormal forces are the friction along the peg. Second, consider friction as the whisker slips along its arc length. Friction in this sense means that the force vector can be nonnormal to the whisker by pointing along the whisker's arc length. The present model constrains the force vector to be perpendicular to the whisker, so it does not account for this type of friction.

Without friction, the mappings between 3D contact point, 3D whisker shape, and  $[\mathbf{F}, \mathbf{M}]$  at the base are all essentially one-to-one. There is a bifurcation in the solution, but the nonphysical result is easy to identify (Hires et al. 2013). With friction, the mappings between 3D whisker shape and  $[\mathbf{F}, \mathbf{M}]$  at the base remain one-to-one, but many different 3D whisker shapes can be associated with the same contact point (the mappings are many-to-one). Therefore, including friction in the model would change the predicted whisker shape, which could help reduce the already tiny error in Fig. 3A.

*Model validity, goodness of fit, and sources of error.* At its most fundamental level, the 3D model presented in this work is based on Euler-Bernoulli beam theory, which relates an applied force to a change in curvature. The model increments along the length of the whisker to compute large deflections. This computational approach ensures that the model is valid for all possible quasistatic whisker-peg configurations and for all whisker shapes. In principle, if all experimental limitations and measurement errors could be accounted for, the model would fit the whisker close to within numerical error.

In simulation, varying the whisker diameter and Young's modulus scales the output forces and moments but does not affect model validity or performance in any other way. The present work used typical values for these parameters in an effort to generate the best-scaled forces and moments.

Model validity, however, is different from the goodness of fit (called "error" in Fig. 3) obtained by finding the difference in shape between the model output and experimental data. The goodness of fit between model and experiment will be limited primarily by errors in tracking exact 3D whisker shape and orientation. Additional sources of experimental error may also include dynamic effects (e.g., vibrations), estimation of whisker taper, and frictional effects.

Tracking accuracy will decrease for smaller whiskers and proximal contacts partially obscured by fur. Tracking accuracy will also decrease with the fraction of the whisker that bends (more distal values of  $r_{cp}$ ) and with the magnitude of the bending (related to  $\theta_{cp}$  and  $\varphi_{cp}$  as defined in Fig. 1A). Accord-

ingly, the error trace in Fig. 3B shows that error tends to increase for larger values of  $r_{cp}$ , as well as in the middle of each whisk, when bending is the largest.

It would be misleading, however, to conclude that the model itself has somehow decreased in validity for larger values of  $r_{cp}$ ,  $\theta_{cp}$ , and  $\varphi_{cp}$ . Rather, it should be understood that goodness-of-fit limitations arise predominantly from tracking error, and it is the tracking error that increases with  $r_{cp}$ ,  $\theta_{cp}$ , and  $\varphi_{cp}$ . Therefore, the error shown in Fig. 3 is unique to the particular camera system and configuration and the tracking methodology employed in the present work; error will be different in other laboratories.

*The importance of 3D analysis.* Monitoring whisking behavior in 3D revealed magnitudes of vertical slip during a single whisk that ranged between 18  $\mu\text{m}$  and 17 mm (Fig. 2, A and B) and speeds between 2.9 and 600 mm/s (Fig. 2, D and E). A full determination of the mechanical conditions that cause large 3D motion requires more investigation and is likely to be complicated by frictional effects. We can state with certainty, however, that in part because the 2D plane of the whisker is not the same as the 2D plane of whisking motion, there will be many whisking situations in which 3D mechanics is significant.

The 3D motion of the whisker will have a large effect on deflection direction (Fig. 4), which is particularly important given that trigeminal ganglion neurons are well known to exhibit strong angular tuning (Jones et al. 2004; Leiser and Moxon 2007; Lichtenstein et al. 1990) and can even appear to change from slowly to rapidly adapting depending on deflection direction (Jones et al. 2004).

Strong directional tuning is maintained throughout the trigeminal pathway (Furuta et al. 2006; Hemelt et al. 2010; Simons 1978, 1985), so 3D mechanics will have a pervasive effect on neural responses throughout the vibrissal-trigeminal system. Studies of S1, for example, demonstrate that deflection direction strongly modulates the neural response to both stimulus amplitude and stimulus speed. The large speeds associated with some vertical slips (Fig. 2, D and E) may be particularly salient cues for cortical neurons sensitive to high velocities and accelerations, noting that both these kinematic variables have directions associated with them (Simons 1978, 1985).

Another important 3D effect is that the intrinsic curvature of the whisker will often cause it to twist about its own axis, generating a twisting moment ( $M_x$ ) that is neglected in 2D analyses. The twisting motion may couple with the kinematic roll previously described (Knutsen et al. 2008) so as to provide a cue for the rat about the horizontal angle in head-centered coordinates at which the whisker has made contact with an object (Knutsen et al. 2008).

*Considerations for experimentalists.* Tracking the full 3D shape of the whisker is challenging and may not be feasible in many neurophysiological experiments. Four strategies may help minimize 3D effects: 1) placing the top-down camera in the same plane as the pitch of the rat's head will best match the plane of whisker rotation; 2) monitoring vertical contact point position with a second camera will permit the removal of whisks with large vertical slip; 3) ensuring that the whisker fully detaches from the object between whisks will minimize accumulation of 3D effects; and 4) ensuring that the object is as perpendicular as possible to the plane of whisker rotation (as in the present study) will minimize vertical motion.

We anticipate that the present work will ultimately allow neuroscientists to correlate 3D forces and moments at the whisker base with neural signals. These correlations would be the first step toward interpreting the neural responses in the vibrissal-trigeminal system in terms of the primary mechanical variables generated during whisking behavior.

## GRANTS

This work was supported by National Science Foundation (NSF) awards IOS-0818414, CAREER IOS-0846088, and EFRI-0938007 (to M. J. Z. Hartmann). L. A. Huet received support from a Department of Defense, Air Force Office of Scientific Research, National Defense Science and Engineering Graduate Fellowship. C. L. Schroeder was partially sponsored by NSF Integrative Research in Motor Control and Movement Grant DGE-0903637.

## DISCLOSURES

No conflicts of interest, financial or otherwise, are declared by the authors.

## AUTHOR CONTRIBUTIONS

L.A.H., C.L.S., and M.J.Z.H. conception and design of research; L.A.H. and C.L.S. performed experiments; L.A.H., C.L.S., and M.J.Z.H. analyzed data; L.A.H. and M.J.Z.H. interpreted results of experiments; L.A.H. and M.J.Z.H. prepared figures; L.A.H. and M.J.Z.H. drafted manuscript; L.A.H., C.L.S., and M.J.Z.H. edited and revised manuscript; L.A.H., C.L.S., and M.J.Z.H. approved final version of manuscript.

## REFERENCES

- Bagdasarian K, Szwed M, Knutsen PM, Deutsch D, Derdikman D, Pietr M, Simony E, Ahissar E. Pre-neuronal morphological processing of object location by individual whiskers. *Nat Neurosci* 16: 622–632, 2013.
- Boubenec Y, Shulz DE, Debregeas G. Whisker encoding of mechanical events during active tactile exploration. *Front Behav Neurosci* 6: 74, 2012.
- Clack NG, O'Connor DH, Huber D, Petreanu L, Hires A, Peron S, Svoboda K, Myers EW. Automated tracking of whiskers in videos of head fixed rodents. *PLoS Comput Biol* 8: e1002591, 2012.
- Ebara S, Kumamoto K, Matsuura T, Mazurkiewicz JE, Rice FL. Similarities and differences in the innervation of mystacial vibrissal follicle-sinus complexes in the rat and cat: a confocal microscopic study. *J Comp Neurol* 449: 103–119, 2002.
- Etnier SA. Twisting and bending of biological beams: distribution of biological beams in a stiffness mechanospace. *Biol Bull* 205: 36–46, 2003.
- Furuta T, Nakamura K, Deschenes M. Angular tuning bias of vibrissa-responsive cells in the paralemniscal pathway. *J Neurosci* 26: 10548–10557, 2006.
- Hartley R, Zisserman A. *Multiple View Geometry in Computer Vision*. Cambridge, UK: Cambridge University Press, 2003.
- Hartog JP. *Advanced Strength of Materials*. New York: Dover, 1987.
- Hemelt ME, Kwegyir-Afful EE, Bruno RM, Simons DJ, Keller A. Consistency of angular tuning in the rat vibrissa system. *J Neurophysiol* 104: 3105–3112, 2010.
- Hires SA, Pammer L, Svoboda K, Golomb D. Tapered whiskers are required for active tactile sensation. *Elife* 2: e01350, 2013.
- Jones LM, Lee S, Trageser JC, Simons DJ, Keller A. Precise temporal responses in whisker trigeminal neurons. *J Neurophysiol* 92: 665–668, 2004.
- Kaneko M, Kanayama N, Tsuji T. Active antenna for contact sensing. *IEEE Trans Rob Autom* 14: 278–291, 1998.
- Knutsen PM, Biess A, Ahissar E. Vibrissal kinematics in 3d: tight coupling of azimuth, elevation, and torsion across different whisking modes. *Neuron* 59: 35–42, 2008.
- Leiser SC, Moxon KA. Responses of trigeminal ganglion neurons during natural whisking behaviors in the awake rat. *Neuron* 53: 117–133, 2007.
- Lichtenstein SH, Carvell GE, Simons DJ. Responses of rat trigeminal ganglion neurons to movements of vibrissae in different directions. *Somatosens Mot Res* 7: 47–65, 1990.
- Mehta SB, Whitmer D, Figueroa R, Williams BA, Kleinfeld D. Active spatial perception in the vibrissa scanning sensorimotor system. *PLoS Biol* 5: 309–322, 2007.
- O'Connor DH, Clack NG, Huber D, Komiyama T, Myers EW, Svoboda K. Vibrissa-based object localization in head-fixed mice. *J Neurosci* 30: 1947–1967, 2010.
- Pammer L, O'Connor DH, Hires SA, Clack NG, Huber D, Myers EW, Svoboda K. The mechanical variables underlying object localization along the axis of the whisker. *J Neurosci* 33: 6726–6741, 2013.
- Quist BW, Faruqi RA, Hartmann MJ. Variation in young's modulus along the length of a rat vibrissa. *J Biomech* 44: 2775–2781, 2011.
- Quist BW, Hartmann MJ. Mechanical signals at the base of a rat vibrissa: the effect of intrinsic vibrissa curvature and implications for tactile exploration. *J Neurophysiol* 107: 2298–2312, 2012.
- Quist BW, Seghete V, Huet LA, Murphey TD, Hartmann MJ. Modeling forces and moments at the base of a rat vibrissa during noncontact whisking and whisking against an object. *J Neurosci* 34: 9828–9844, 2014.
- Ritt JT, Andermann ML, Moore CI. Embodied information processing: vibrissa mechanics and texture features shape micromotions in actively sensing rats. *Neuron* 57: 599–613, 2008.
- Simons DJ. Response properties of vibrissa units in rat SI somatosensory neocortex. *J Neurophysiol* 41: 798–820, 1978.
- Simons DJ. Temporal and spatial integration in the rat SI vibrissa cortex. *J Neurophysiol* 54: 615–635, 1985.
- Solomon JH, Hartmann MJ. Artificial whiskers suitable for array implementation: accounting for lateral slip and surface friction. *IEEE Trans Rob Autom* 24: 1157–1167, 2008.
- Solomon JH, Hartmann MJ. Extracting object contours with the sweep of a robotic whisker using torque information. *Int J Rob Res* 29: 1233–1245, 2010.
- Solomon JH, Hartmann MJ. Radial distance determination in the rat vibrissal system and the effects of Weber's law. *Philos Trans R Soc Lond B Biol Sci* 366: 3049–3057, 2011.
- Solomon JH, Hartmann MJ. Robotic whiskers used to sense features. *Nature* 443: 525, 2006.
- Szwed M, Bagdasarian K, Ahissar E. Encoding of vibrissal active touch. *Neuron* 40: 621–630, 2003.
- Williams CM, Kramer EM. The advantages of a tapered whisker. *PLoS One* 5: 8, 2010.
- Wolfe J, Hill DN, Pahlavan S, Drew PJ, Kleinfeld D, Feldman DE. Texture coding in the rat whisker system: slip-stick versus differential resonance. *PLoS Biol* 6: 1661–1677, 2008.
- Yan W, Kan Q, Kergrene K, Kang G, Feng XQ, Rajan R. A truncated conical beam model for analysis of the vibration of rat whiskers. *J Biomech* 46: 1987–1995, 2013.